acoustics

MDPI

Article

The Simulation Method for Ultrasonic Non-Destructive Testing of Delamination Defects in CMC Based on Air-Coupled Lamb Waves

Da Kang [1,2,†], Lu Lu [1,†], Zhenggan Zhou [1], Yunmiao Zhang [2], Hong Zhang [2] and Wenbin Zhou [1,*]

[1] School of Mechanical Engineering and Automation, Beihang University, Beijing 100083, China; kang_dandt@buaa.edu.cn (D.K.); lulull@buaa.edu.cn (L.L.); zzhenggan@buaa.edu.cn (Z.Z.)
[2] Beijing Power Machinery Research Institute, Beijing 100074, China; dqzym97@163.com (Y.Z.); zh31sbuaa@163.com (H.Z.)
* Correspondence: zhouwb@buaa.edu.cn
† These authors contributed equally to this work.

Abstract

Ceramic Matrix Composite (CMC) are widely used in aerospace due to the advantages such as high-temperature resistance and lightweight properties. Detecting defects within these materials is crucial for ensuring the safety of corresponding structures. In this paper, a finite element model of CMC model for layered structures is established for the ultrasonic non-destructive testing. Based on the computed tomography (CT) scan images and porosity of the material, a randomly distributed pore model is constructed to investigate the effect of pores on the ultrasonic signals. Random pores are also introduced in the simulation to ensure that the model corresponds as closely as possible to reality. Moreover, the feasibility of utilizing air-coupled ultrasonic excitation to generate specific frequency Lamb waves is verified. The effect of pore presence on the signal propagation is analyzed, and the effects of layered structures at different positions and lengths on the signal propagation are investigated. The results demonstrate that the Lamb waves with a specified frequency can be excited using the method described in this paper, and the presence of pores and delamination defects can affect the propagation of the Lamb wave in CMC, in which the signal attenuation can reach up to 7.6 dB.

Keywords: Lamb wave; Ceramic Matrix Composites; pore model; delamination defects

1. Introduction

Ceramic matrix composite (CMC) possess outstanding properties such as high-temperature resistance, high specific strength, high specific modulus, oxidation resistance, and ablation resistance. Consequently, they are widely used in aerospace applications including engine nozzles and spacecraft thermal protection system [1–3]. Due to complex manufacturing processes and micro-structural characteristics involving multiple phases, CMC is particularly prone to developing various defects during production, such as porosity, inclusions, cracks, and interfacial delamination. These defects not only compromise the material's initial properties but my also precipitate more severe safety issues during subsequent service. Generally speaking, CMC is commonly constructed as bonded structures. During material fabrication and practical application, incomplete bonding or bonding failure frequently leads to the presence of delamination defects [4,5]. Thus, it is essential to conduct non-destructive testing on CMC to ensure the secure operation of equipment.

Check for updates

Received: 27 April 2026
Revised: 31 May 2026
Accepted: 2 June 2026
Published: 5 June 2026

 https://doi.org/10.3390/acoustics8020038

In conventional non-destructive testing methods, ultrasonic detection possesses advantages such as strong penetration capability, high efficiency, and low cost, making it widely applied in industrial settings [6,7]. In practical application, as CMC exhibit poor surface quality and contain pores, the material is unsuitable for immersion in water. Furthermore, it proves difficult to thoroughly clean the surface coupling agent, making conventional ultrasonic testing challenging [8,9]. In consideration of this characteristic set of materials, employing non-contact air-coupled sonic testing for non-destructive testing of CMC represents an effective methodology [10].

Compared to body wave testing, which can only examine the area directly below the transducer, the use of Lamb waves for non-destructive testing enables a single-pass inspection of the entire material [11–13]. Furthermore, in the inspection of thin plates or composite laminates, bulk waves are susceptible to interference from multiple reflections in the thickness direction, resulting in blind zones during the inspection process. In contrast, guided waves propagate within thin plates, forming coherent wave fields through the combined effects of boundary conditions, multiple reflections, and interference. Consequently, the guided wave represents the optimal choice for large-area inspection of thin-walled components [14–16]. In the early stages, a visualisation technique capable of simultaneously determining both group velocity and phase velocity was proposed. It was successfully applied to the visualisation technique of Lamb waves, thereby obtaining the phase velocity and group velocity of Lamb wave propagation. Subsequently, these measurements were applied to the phase velocity and group velocity of Lamb wave propagation within steel pipes and steel pressure vessels [17]. Subsequently, a method for exciting and receiving slow ultrasonic A_0 mode Lamb waves propagating within plastic films was proposed, and it was noted that this technique could be employed in developing novel air-coupled ultrasonic non-destructive testing based on subsonic guided waves [18]. Researchers have investigated the influence of droplets on the surface of test plates upon the propagation of air-coupled waves, as well as analyzed the oscillatory behavior of Lamb waves. Consequently, it has been demonstrated that Lamb waves can be generated through a non-contact mechanism [19]. In the field of air-coupled ultrasonic testing in CMC, the mechanical properties and microstructure of CMC were evaluated using air-coupled ultrasound. The local acoustic damping of CMC panels obtained from air-coupled ultrasonic analysis was correlated with destructive mechanical testing and microstructural analysis, demonstrating that air-coupled ultrasonic is highly sensitive to submicron-level cracks and elated interlayer properties in CMC [20]. Research has found that through non-destructive air-coupled ultrasonic testing, the most prominent defects identified are layered regions exhibiting unique responses when interacting with acoustic waves. The influence of porous regions within CMC on acoustic wave propagation has also been investigated [21]. However, current numerical simulations of non-destructive testing for CMC are based on idealised models, which overlook the impact of the inherent porosity in the material on the test results. Consequently, the simulation results fail to provide sufficiently accurate guidance for practical applications.

In this context, non-destructive testing of delamination defects in CMC plates containing voids using air-coupled guided waves is investigated by numerical simulation. Firstly, a finite element model of a CMC plate with a laminated structure containing random pores is established. The dispersion characteristics of this CMC plate are analyzed, and an excitation model for the corresponding A_0 mode Lamb wave is developed. Subsequently, the excitation of the A_0 mode Lamb wave is verified, and the influence of porosity on signal propagation is investigated. Finally, the delamination defect of varying lengths and positions are introduced into the model, and the detection capability of air-coupled excitation Lamb waves for delamination defects is investigated.

https://doi.org/10.3390/acoustics8020038

2. Finite Element Model of CMC with Pores

The CMC are composite materials consisting of a ceramic matrix reinforced with various fibers, typically consolidated into final components through the spatial stacking of unidirectional plies [22]. In numerical simulations, the CMC are simplified as a laminate structure. In this paper, the signal is modeled using a 0° and 90° cross-layered approach, as shown in Figure 1. Directions x and y represent the fiber orientation, while direction z corresponds to the material thickness. Directions x and y exhibit similar properties and are isotropic planes. In this study, the model satisfies the long-wavelength approximation. The CMC composites can be regarded as transversely isotropic materials.

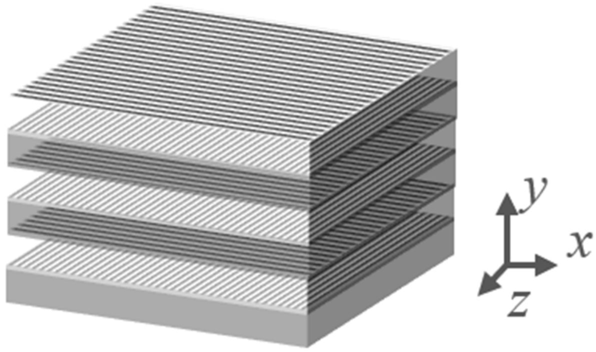

Figure 1. Schematic diagram of the CMC layered structure.

In the simulation, a numerical model is established using COMSOL Multiphysics. Based on experimental measurements, the material density is determined to be 2100 kg/m^3. The elastic matrix of the material at 0° is defined by Equation (1). To correspond with the physical model, a composite structure comprising 20 layers is simulated. This structure featured a symmetrical configuration formed by alternating 0° and 90° layer orientations, with each layer measuring 0.2 mm.

$$[c_{ij}] = \begin{bmatrix} 109.24 & 26.28 & 17.54 & 0 & 0 & 0 \\ 26.28 & 109.24 & 17.54 & 0 & 0 & 0 \\ 17.54 & 17.54 & 6.8 & 0 & 0 & 0 \\ 0 & 0 & 0 & 13.93 & 0 & 0 \\ 0 & 0 & 0 & 0 & 13.93 & 0 \\ 0 & 0 & 0 & 0 & 0 & 34.783 \end{bmatrix} \text{GPa} \quad (1)$$

In numerical modeling, CT (Computed Tomography) scans are performed on specimens to fully account for the microstructural characteristics of materials and enhance the accuracy of the model. The results obtained are shown in Figure 2. It is clearly shown in the figure that there are numerous pores within the material, exhibiting an irregular distribution pattern. The porosity of the specimen is calculated as 23% by summing the areas of the porous regions and the sample area by Volume Graphics. According to the statistics, the largest pore size is 0.2 mm and the smallest is 0.05 mm. Consequently, this paper applies COMSOL Multiphysics modelling to establish a structure with randomly pores distributed throughout the material. The pore locations are randomly generated, and their shapes are randomly selected from square, circular, or elliptical configurations and appear with equal probability. The maximum pore size is set at 0.2 mm while the minimum pore size is 0.05 mm, and maintaining a constant porosity throughout the material. The detailed view of the model is shown in Figure 3.

https://doi.org/10.3390/acoustics8020038

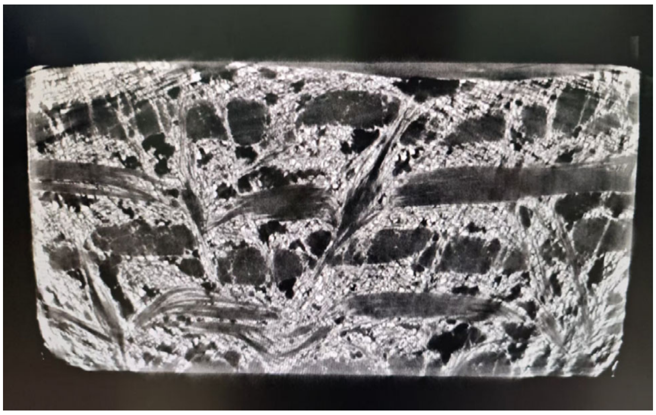

Figure 2. The CT scan of CMC.

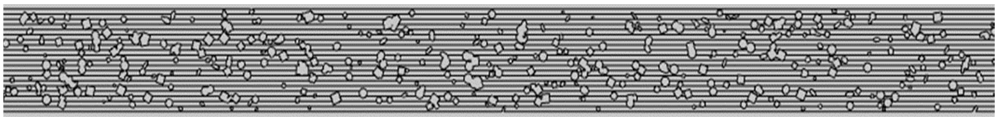

Figure 3. The detailed view of the finite element simulation of CMC.

3. Finite Element Model Development for Air-Coupled Guided Wave Detection

Based on the construction of a two-dimensional finite element model for multilayer CMC plates, it is necessary to establish an excitation and reception model for air-coupled ultrasonic guided waves for numerical simulation. In this paper, Snell's law is utilized to excite air-coupled guided waves via oblique incidence, which requires the characterization of the dispersion curve of the guided wave within the material [23]. Based on material properties, the dispersion curves for CMC materials with 20 layers, 0° and 90° cross-layers are plotted by the software of Dispersion Calculator 3.0, as shown in Figure 4.

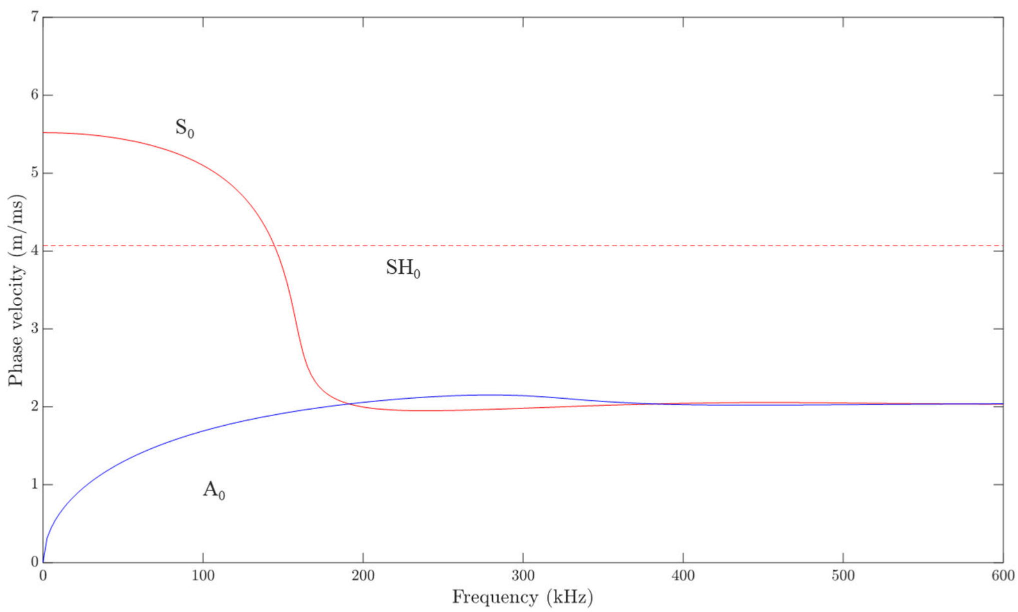

Figure 4. The dispersion curve of CMC.

It can be observed from the phase velocity curve that when the signal frequency exceeds 200 kHz, the phase velocities of the A_0 mode and S_0 mode of Lamb waves are similar in magnitude, making the two modes hard to distinguish. There for, to ensure purer and more easily analyzable signals in the simulation, a 100 kHz signal is adopted for this study. The phase velocity curve indicates that the phase velocity of the 100 kHz Lamb wave propagating through the CMC plate established in this study is 1689.92 m/s, while its group velocity is 2569.2 m/s. The propagation speed of sound waves in air is 340 m/s. According to Snell's law, the incident angle for exciting the A_0 mode Lamb wave in the CMC plate from air is 11.61°. An excitation model for air-coupled ultrasonic Lamb waves, illustrated in Figure 5, is established.

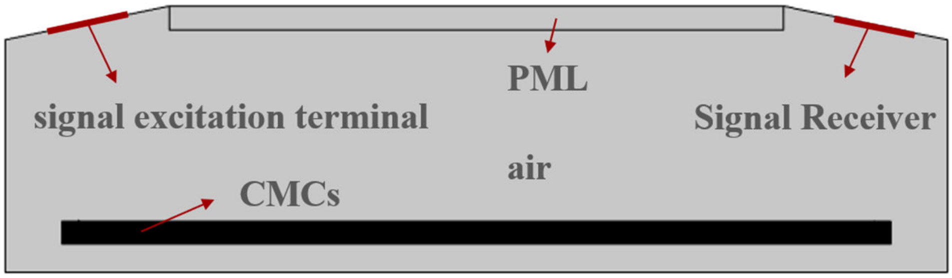

Figure 5. Air-coupled ultrasonic lamb wave excitation model.

The air-coupled ultrasonic Lamb wave excitation model primarily consists of an air segment as the main excitation component. The material is set to air to simulate the propagation of the acoustic field within the air medium in air-coupled ultrasonics. In the air domain, a transmitting section and a receiving section, both 10 mm in length, are positioned on opposite sides of the plate to transmit and receive ultrasonic Lamb wave signals, respectively, according to the required excitation and reception angles. Additionally, the CMC model established earlier is incorporated into the air section, with its length adjustable according to detection requirements. A perfectly matched layer (PML) is configured at the top of the air section to absorb ultrasound waves reflected into the air, ensuring that reflected spurious signals do not interfere with the analysis of results. Similarly, PML is also installed at both edges of the CMC panel to ensure the signal purity as much as possible. In order to effectively suppress numerical dispersion and improve signal accuracy, and taking into account the available computational resources, the mesh is subdivided into 1/10 of the wavelength during the simulation. During the calculation process, adaptive mesh refinement is also applied around the pores to ensure computational accuracy, the minimum mesh size near small pores is approximately 0.002 mm.

To verify whether the model can induce the target A_0 mode lamb wave, the propagation distance of the signal within the plate is adjusted to 100 mm and 120 mm, while all other conditions remained the same. Then the group velocity of the signal propagation within the plate is calculated using the collected data.

The schematic diagram of sound field propagation in air is shown in Figure 6. It can be clearly observed from the figure that the acoustic waves emitted by the ultrasonic transducer propagate outward in air as near-spherical waves before reaching the plate. Simultaneously, it is evident that the strength of the signal significantly weakens after passing through the PML. Thus, the presence of the PML effectively suppresses the generation of noise within the signal, playing a crucial role in subsequent signal processing. The Figure 7 shows the stress distribution of signals in the CMC plate. The figure reveals a periodically distributed displacement concentration pattern along the plate's propagation path. Based on Lamb wave propagation theory, it can be determined that the Lamb waves of a specific order were excited.

https://doi.org/10.3390/acoustics8020038

Figure 6. Cloud diagram of sound pressure in the air.

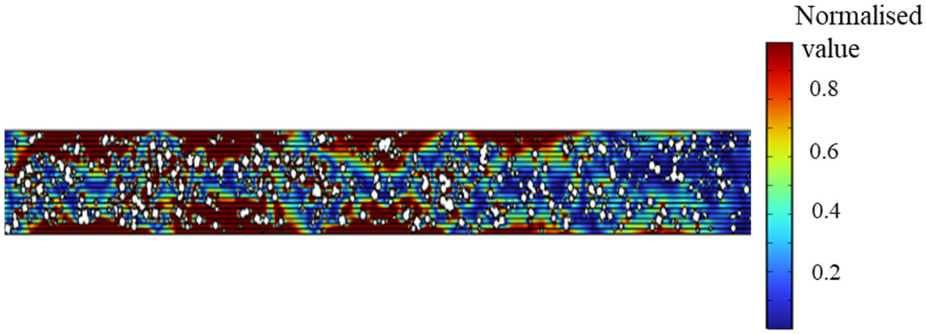

Figure 7. Stress distribution diagram of signals in CMC with porosity of the specimen of 23%.

The time-domain diagram of the signal received at the receiver at a propagation distance of 100 mm is shown in Figure 8. As seen in the figure, the amplitude remains at 0 from 0 to 2.4×10^{-4} s, indicating that no wave reached the monitoring point during the initial simulation phase. The propagation time of the A_0 mode Lamb wave from excitation to the receiving point in the model is calculated to coincide with the signal appearance time in the time-domain plot. The first relatively complete signal detected is identified as the A_0 mode Lamb wave required for the study. The propagation distance of the acoustic wave within the plate is adjusted to 120 mm to calculate the group velocity of the wave propagating through the material.

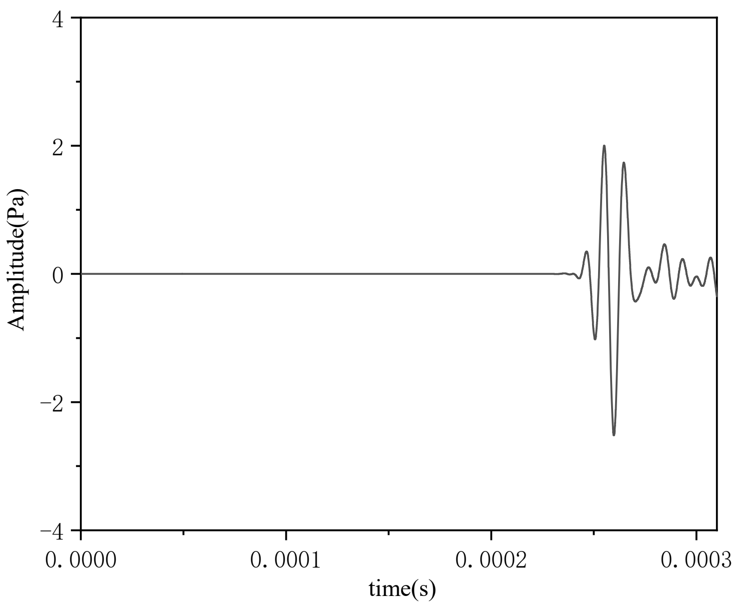

Figure 8. Timed domain signal at a propagation distance of 100 mm with porosity of the specimen of 23%.

https://doi.org/10.3390/acoustics8020038

The time-domain diagrams of the received signals at propagation distances of 100 mm and 120 mm are plotted on a single graph, as shown in Figure 9. It is clearly visible from the figure that the waveform remains consistent across different propagation distances, though the arrival times of the wave packets are different. Based on the transmission time of the wave, the group velocity of the received signal is calculated to be 2.395 m/ms. Considering the presence of pores in the material, scattering of signals within the plate may occur, resulting in measured group velocities being lower than theoretical values. Therefore, within acceptable error limits, the simulated group velocity can be considered consistent with theoretical values, indicating that A_0 mode Lamb wave signals can be excited using the model established in this simulation.

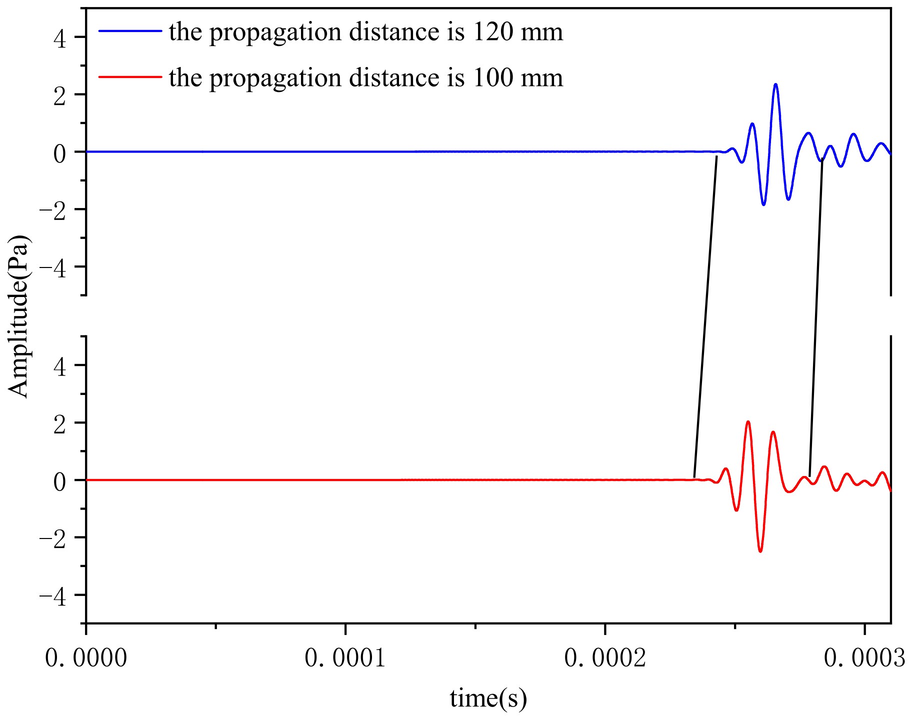

Figure 9. Time domain signal at different transmission distances with porosity of the specimen of 23%.

In addition to determining the mode of the signal based on group velocity, further mode analysis of the signal is carried out in the numerical simulation by analyzing the signal in frequency spectral. A fast Fourier transform is applied to the signals received at a propagation distance of 100 mm, the frequency spectrum of the signals is shown in Figure 10. As can be seen from the figure, the centre-frequency of the signals is mainly concentrated at 100 kHz, which is consistent with the excitation frequency mentioned above. Moreover, probes are positioned at 0.1 mm intervals between 80 mm and 100 mm to receive the signal, and analysis is conducted on the frequency-wavenumber domain.

Figure 11 shows the frequency-wavenumber plot of the received signal, along with the theoretical frequency-wavenumber curves for the A_0 and S_0 mode signals of the plate. As can be clearly seen from the figure, the frequency of the received signals is mainly concentrated around 100 kHz, and is clustered near the theoretical frequency-wavenumber diagram for the A_0 mode. The phenomenon indicates that the presence of pores in the model cannot induce the mode transition, the signals propagating through the plate remains the A_0 mode Lamb wave, and it can be employed for subsequent research.

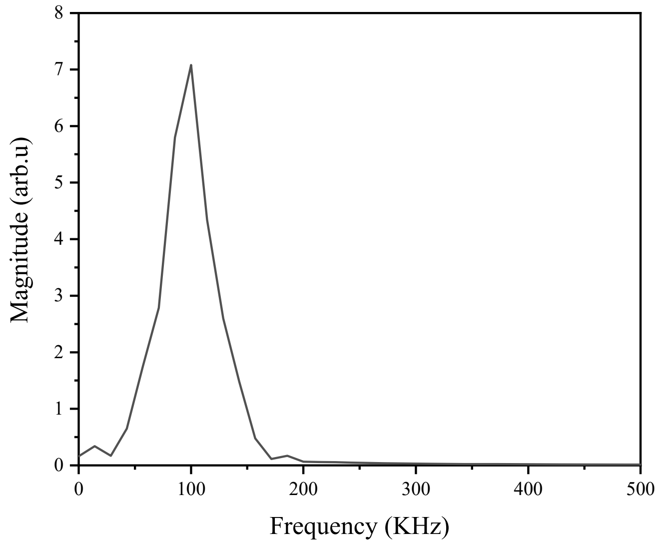

Figure 10. Frequency spectrum of the received signals.

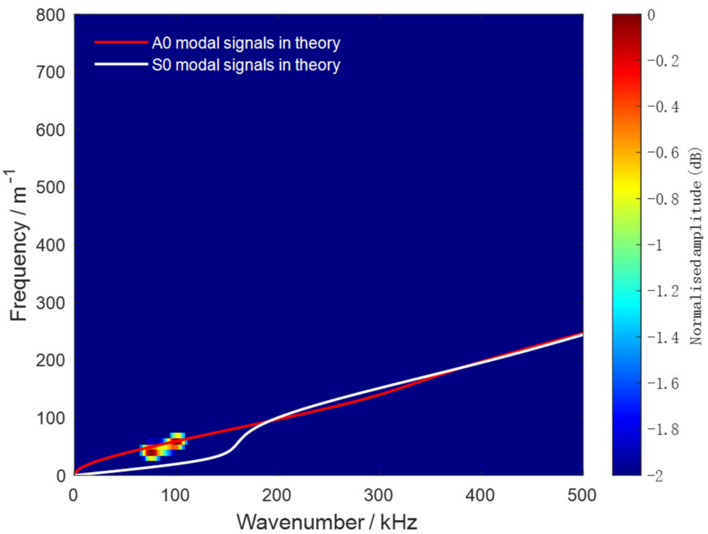

Figure 11. Frequency-wavenumber of the received signal and theoretical values.

4. Results and Data Processing

In conducting layered defect detection for CMC using guided waves, the primary considerations involve the effects of defect length and depth on signal propagation. Based on the previously described guided wave excitation model, propagation of guided waves in CMC plates with and without voids is investigated, and simulation studies are established for delamination defects of different positions and lengths.

4.1. The Effect of Pore on Guided Wave Propagation

To investigate the effect of pore structure on Lamb wave propagation, this section begins with comparative simulations of Lamb wave propagation in both porous and non-porous conditions. The parameters and methods are consistent with those in Section 3, with the single difference lying in whether the CMC material contains pores. The CMC plate with pores is shown in Figure 3 above, while the CMC model without defects is shown in Figure 12.

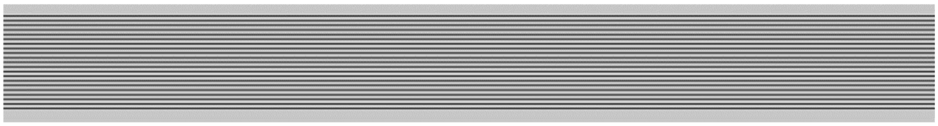

Figure 12. Complete CMC partial simulation model.

A detailed view of the stress distribution map for Lamb waves propagating in the plate is shown in Figure 13. As shown in the figure, within an ideal void-free medium, the acoustic wave exhibits a regular, continuous, and highly periodic wave structure with a uniformly distributed stress field. This indicates that guided waves can maintain stable mode characteristics for long-distance propagation. When randomly distributed pores are introduced into the medium, multiple scattering and mode conversion effects occur in Lamb waves due to acoustic impedance mismatch between the pores and the matrix material, resulting in disordered stress distribution patterns.

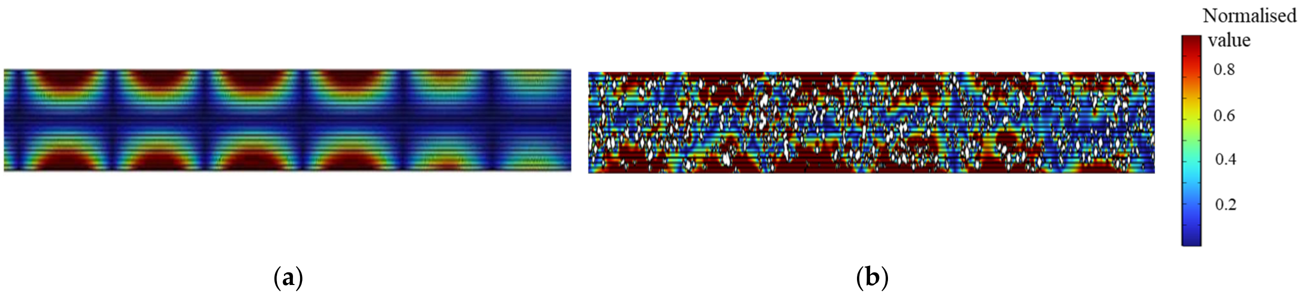

Figure 13. Stress contour map, (**a**) without pores, (**b**)with pores.

Figure 14 shows the time-domain signals with and without pores. It can be observed that the amplitude peak of the porous signal decreases compared to the non-porous signal, and the signal with pores appears later than that of the completely non-porous plate. This is due to the presence of pores causing the dispersion of signals, which in turn alters the group velocity of Lamb wave propagation, resulting in a delayed arrival time for the received signal.

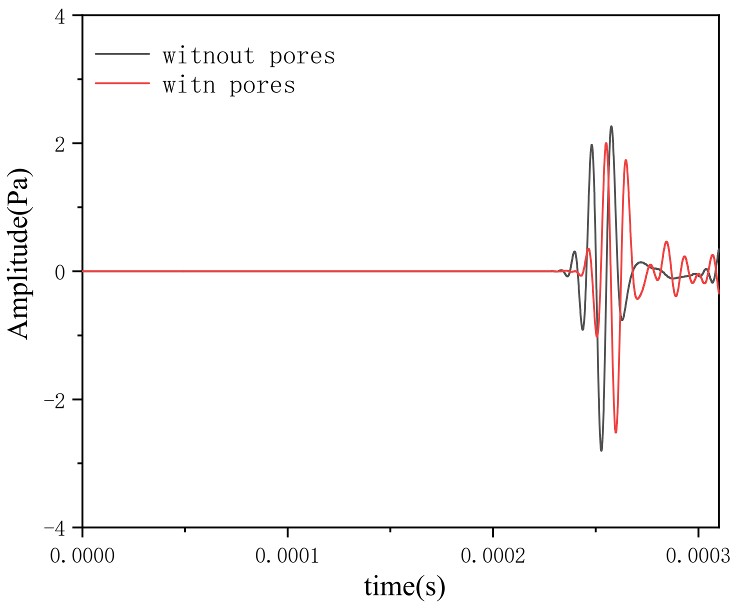

Figure 14. Time domain signal with and without pores.

Based on the aforementioned research, and to ensure the generalisability of the simulation results, further investigation is required into the effects of various randomly generated pore models on signal propagation. Thus, employing the pore generation method described above and maintaining a porosity of 23% constant, ten different pore models are generated for simulation. Enlarged views of the pores in ten models are shown in Figure 15.

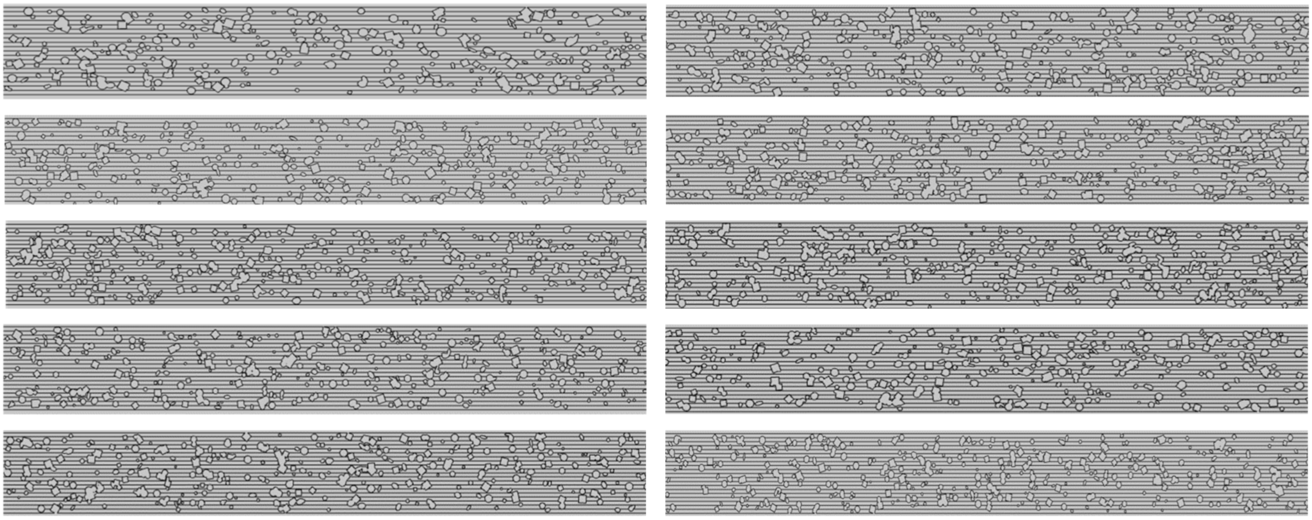

Figure 15. A comparison of ten different pore models.

Simulations using ten randomly generated pore models, the received time-domain signals are shown in Figure 16. As illustrated in the figure, the amplitude and the appearance time of the Lamb wave received from the ten models show little variation. A statistical analysis is conducted on the maximum amplitude and timing of received signals across different models. Figure 17 shows the distribution of standard deviations of the d peak amplitudes and the arrival times. The maximum amplitude has a mean value of 2.533 and a standard deviation of 0.1341 and the arrival time has a mean value of 2.607×10^{-4} s and a standard deviation of 6.377×10^{-7} s, the variances of which are relatively small. Thus, within the permissible margin of error, the signals propagate in the 10 models can be regarded as consistent.

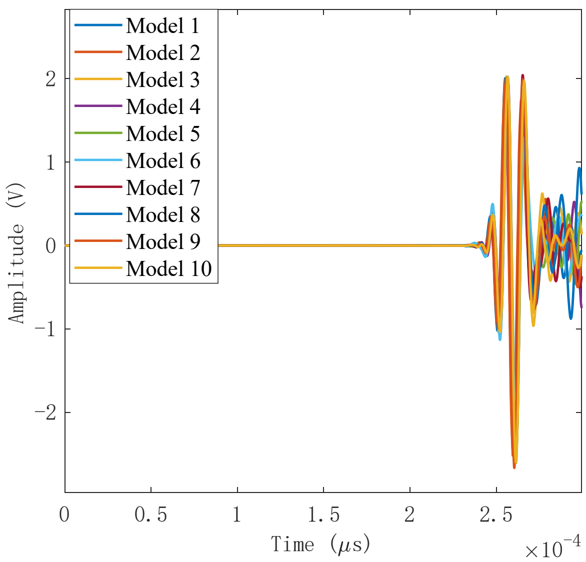

Figure 16. Time-domain signals received under different pore models.

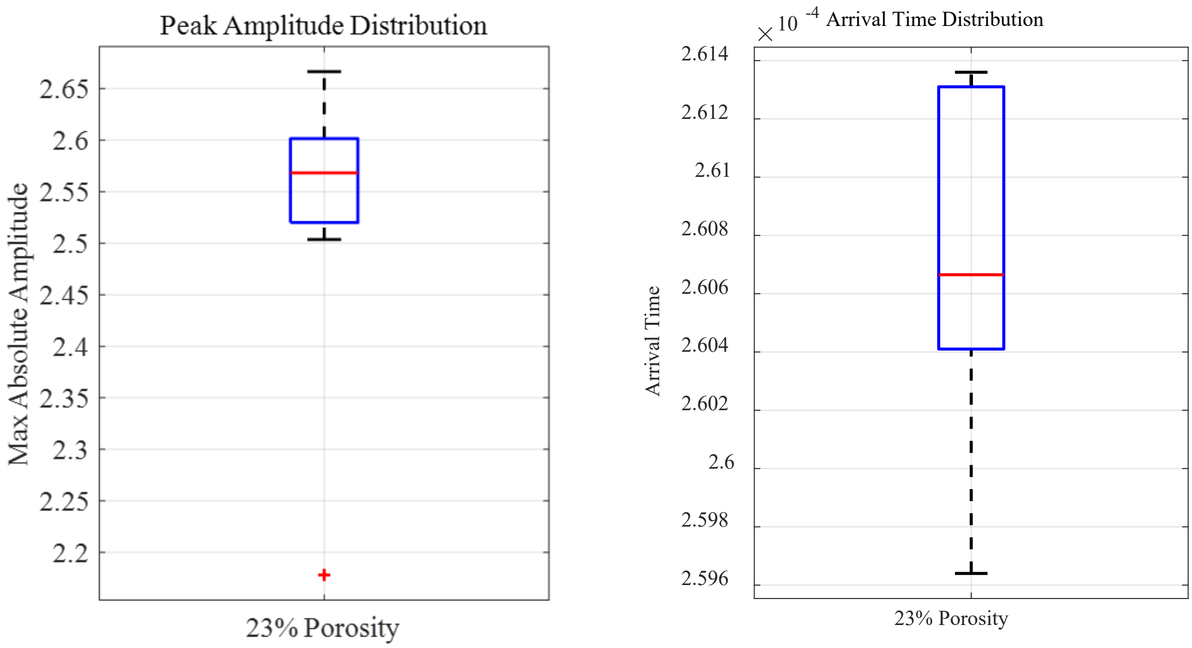

Figure 17. Standard deviations of the peak amplitudes and arrival times.

It can be inferred that, for a given porosity, the size of individual pores and the pore distribution have little effect on the propagation of Lamb waves, and different pore models have the same impact on signal propagation. Thus, it is demonstrated that the results remain generally applicable whether any pore model is used in the simulation process.

4.2. Effect of Length of Delamination Defects on Propagation of Air-Coupled Guided Wave

To investigate the effect of delamination defects of varying lengths on Lamb wave propagation, simulations incorporating delamination defects are conducted based on the above model. The width of the delamination defect is fixed at 0.2 mm, as shown in Figure 18. During the simulations, all other conditions remained constant. During the simulation process, while keeping all other conditions constant, calculations are performed by varying the length of the layered defect to 6 mm, 8 mm, and 10 mm respectively.

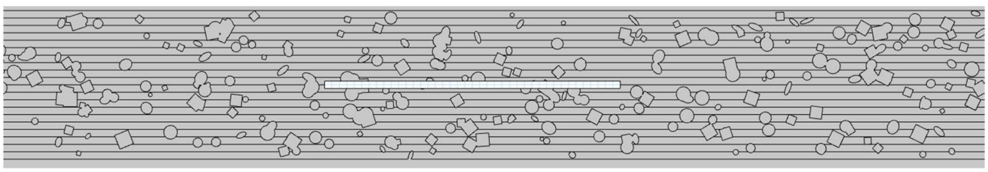

Figure 18. Diagram of delamination defects defects.

As the guided wave signal propagates near a layered defect, the stress distribution within the plate is illustrated in Figure 19. Around the defect, the stress field becomes less pronounced, and the intensity of the signal is weakened. Due to the layered defect, the originally uniform thickness of the single-layer board is divided into two distinct thicknesses. Such a change in Frequency-Thickness Product causes a mismatch in the phase velocity of the excitation signal. Similarly, during the signal reception process, the angle of the receiving probe is optimized for the phase velocity of intact material. Changes in phase velocity within the defect area cause deflection of the corresponding receiving angle, preventing the receivers from achieving the optimal reception direction. As a result, signal strength experiences a significant reduction.

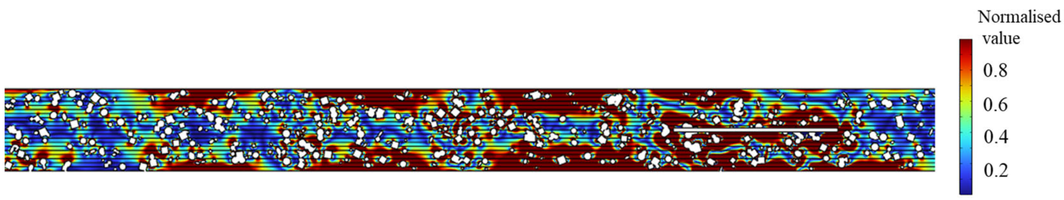

Figure 19. Stress contour map of the signals with layered defects.

The signals received from the intact plate and those received in the presence of delamination defects measuring 2 mm wide and 6 mm, 8 mm and 25 mm long, respectively, is plotted at Figure 20. As seen in the figure, the signals suffer significant attenuation with the presence of delamination defects. The longer the delamination length, the more pronounced the signal attenuation.

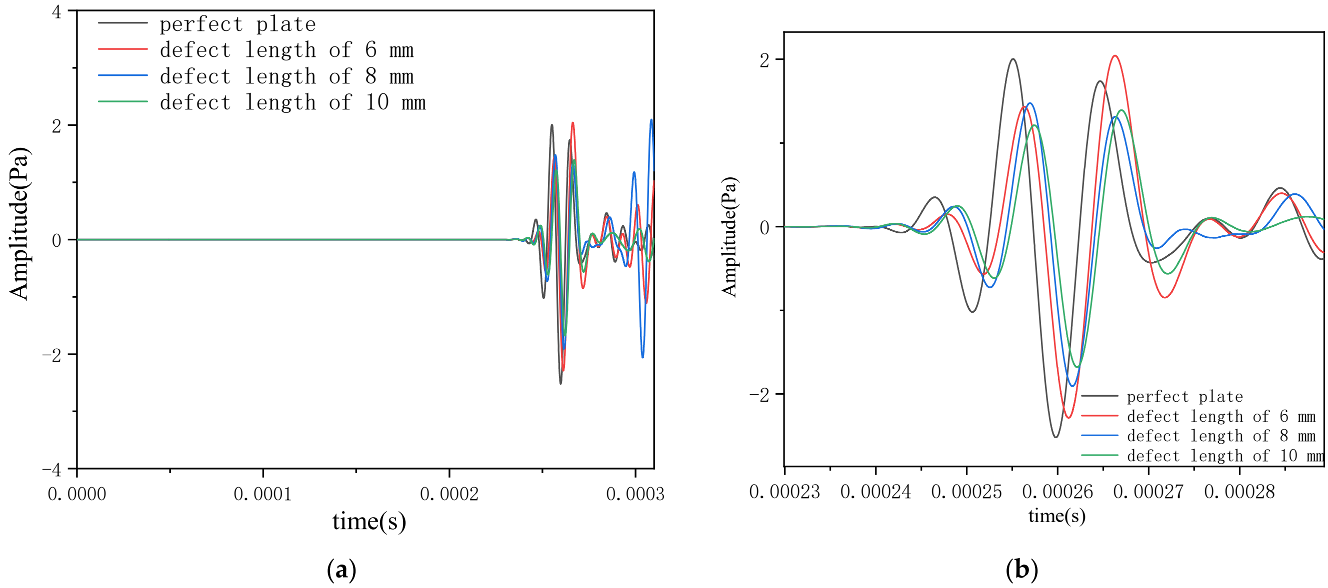

Figure 20. Time-domain signals under different conditions (perfect plate and the defect length of 6, 8 and 10 mm), (**a**) original image, (**b**) magnified section.

In practical non-destructive testing applications, it is necessary to ensure that signals exhibit significant attenuation when defects exist to facilitate observation. Based on this principle, trapezoidal rule is employed in this paper to process the signals [24]. The principle of the Trapezoidal Integration Processing lies in approximating signal curves using linear segments. It approximates signal changes between adjacent sampling points as straight line segments, forming continuous trapezoidal regions. By accumulating the areas of these trapezoids, it approximates the true integral value, converting signal variations into cumulative quantities. As a result, changes in the signal become more pronounced.

The results of signal processing under different-length delamination defects using Trapezoidal Integration Processing are shown in Figure 21. This processing method can be precisely located to the minimum value where the signal appears, laying the groundwork for subsequent signal processing.

After processing the results obtained from trapezoidal integration, the detrend function is applied to remove trends from the signal, minimizing the impact of noise on the signal. Subsequently, the convCal function is used to perform convolution autocorrelation processing on the signal, to extract its energy distribution characteristics. The final time-domain signals are shown in Figure 22. Compared to the original signal, the processed signal shows a more pronounced attenuation trend relative to the defect signal. It demonstrates that the signal processing method described previously enables more precise identification of defect signals.

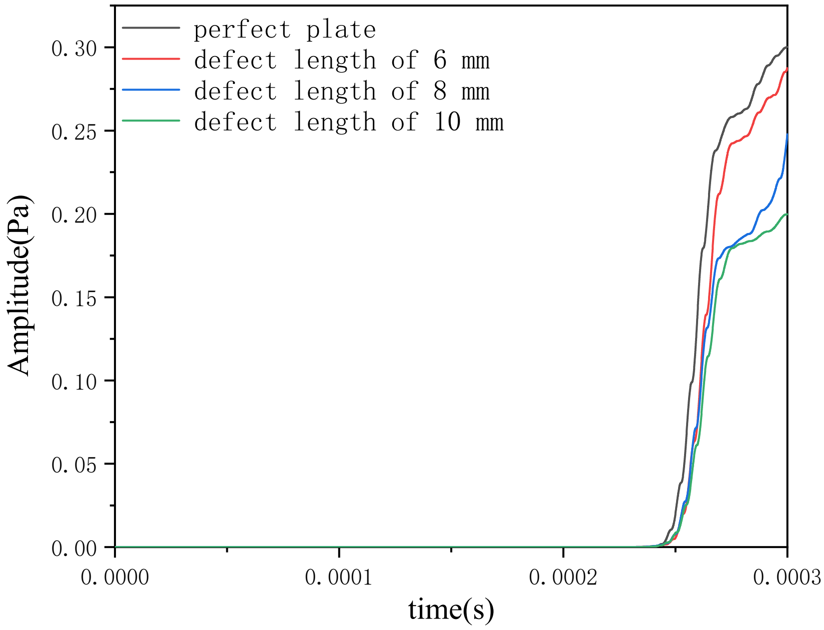

Figure 21. Signal after trapezoidal integration processing (perfect plate and the defect length of 6, 8 and 10 mm).

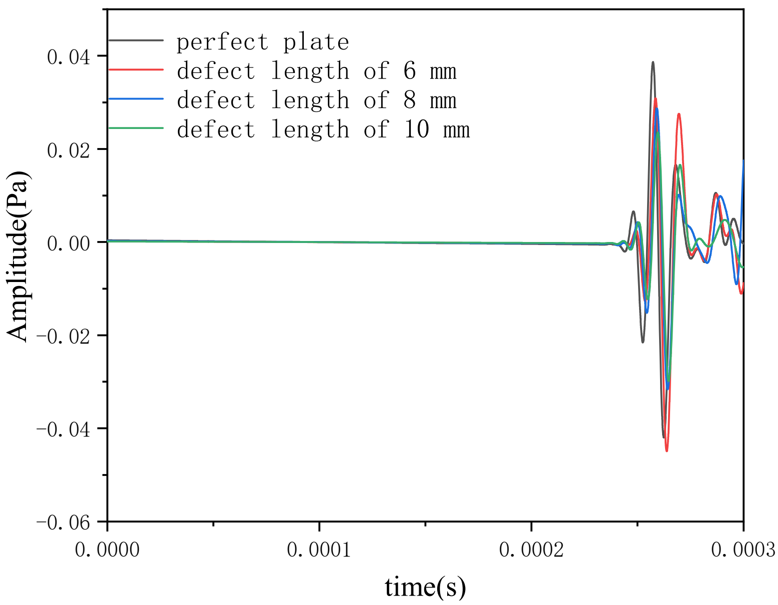

Figure 22. Time-domain signal after convolution processing (perfect plate and the defect length of 6, 8 and 10 mm).

Based on the signals in the non-defective plate, the signal attenuation values at different layered lengths are calculated using the following equation:

$$\beta = 20\lg\frac{P_1}{P_2} \tag{2}$$

P_1 represents the maximum amplitude of the reference signal; P_2 represents the maximum amplitude of the signal in the complete plate. β is the attenuation value of the signals.

The results are shown in Table 1, and the corresponding relationship of attenuation values and defect length is shown in Figure 23. As shown in the figure, the degradation value of the signal increases linearly with the length of the defect. After applying the signal processing described in this paper, the degradation becomes even more noticeable. It is demonstrated that the method proposed in this paper can be applied to detect delamination defects in CMC plates containing pores, and it exhibits high detection sensitivity. At the same time, the application of the signal processing methods described in this paper can more effectively highlight the impact of defects of different lengths on Lamb wave, thereby making the detection results more obvious.

Table 1. Signal attenuation value.

	6 mm	**8 mm**	**10 mm**
Original signal	0.8310 dB	2.4197 dB	3.5208 dB
Following the autocorrelation process	0.9015 dB	4.9612 dB	7.5994 dB

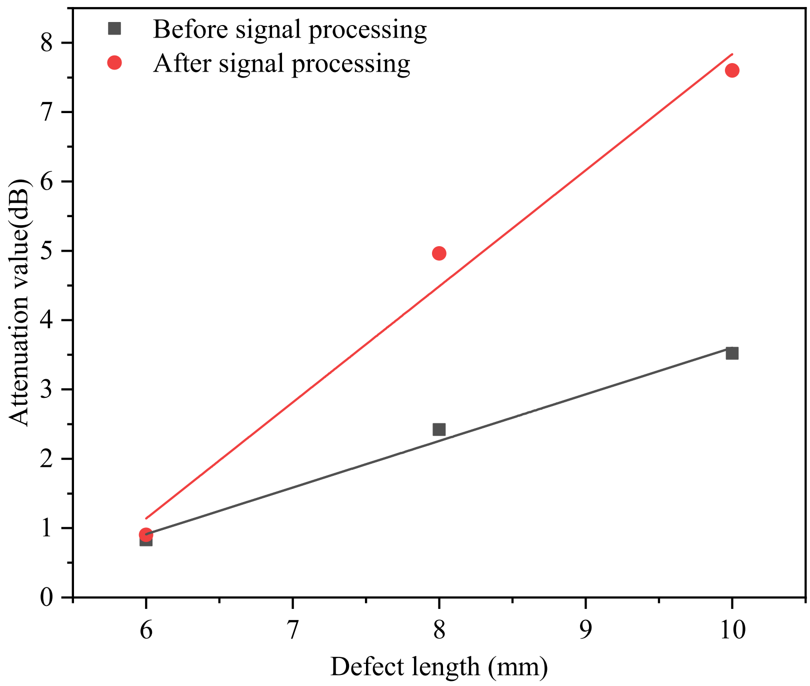

Figure 23. The relationship of attenuation values and defect length.

4.3. The Effect of Location of Delamination Defects on the Propagation of Air-Coupled Guided Waves

Following research into the effect of layered defect length on Lamb wave propagation, and based on engineering practice requirements, the present study further investigates the influence of the layered position on Lamb wave propagation. In theory, the presence of delamination defects alters the propagation conditions for Lamb waves, effectively dividing the plate into two sections. Delamination defects positioned symmetrically relative to the midpoint exert identical effects on signal propagation. Accordingly, a study is conducted using a model with two symmetrically positioned layered defects. The defect width remains constant at 8 mm and 0.2 mm respectively, located symmetrically at distances of 1.4 mm and 2.6 mm from the top surface of the plate. A magnified view of the layered defect section in the established model is shown in Figure 24.

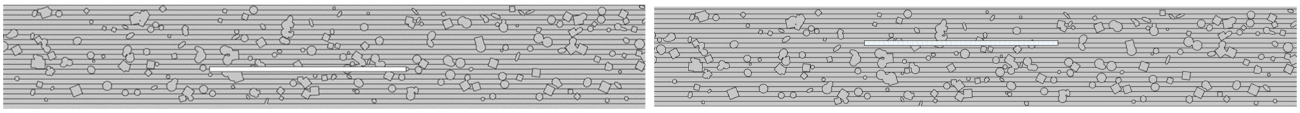

(**a**) (**b**)

Figure 24. Schematic diagram of the model at different stratification positions from the surface, (**a**) delamination at 2.6 mm, (**b**) delamination at 1.4 mm.

The stress contour map when the signal passes near the defect is shown in Figure 25. It can be observed that when the delamination is located in the upper region of the plate thickness, the defect interface divides the complete waveguide structure into two sections: a thinner upper part and a thicker lower part. These two regions respectively generate two Lamb wave signals propagating at different velocities. Furthermore, the stress contour maps near the delamination defects at the two symmetrical positions exhibit highly symmetrical consistency.

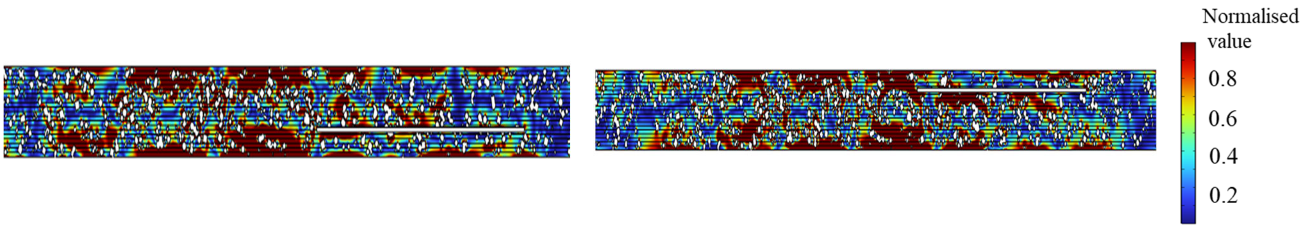

(**a**) (**b**)

Figure 25. Stress Contour Map of the Signal at different stratification positions from the surface, (**a**) at 2.6 mm, (**b**) at 1.4 mm.

The time-domain signals received at the two aforementioned positions are plotted in a single graph, as shown in Figure 26. Although the two signals do not perfectly coincide, within the permissible error range, the time-domain waveforms exhibit an exceptionally high degree of consistency in terms of packet arrival time and overall amplitude envelope. This phenomenon provides direct empirical validation that the layered defect situated at the symmetrical position of the intermediate surface geometry consistently influences the propagation of Lamb waves.

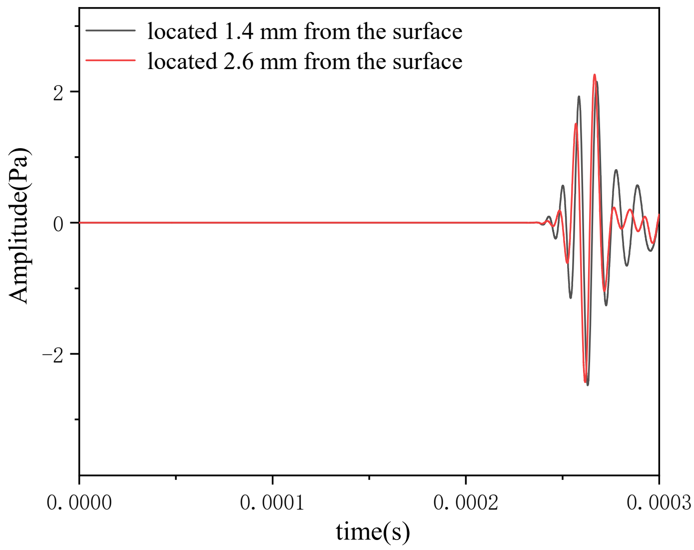

Figure 26. Time-domain Signal of two symmetrical positions (1.4 mm and 1.6 mm from the surface respectively).

Building upon the aforementioned research, simulations are conducted with delamination defects positioned at various locations. Considering symmetry and the total plate thickness of 4 mm, the laminated positions are confined to the range between 0 mm and 2 mm from the lower plate surface. Specifically, defects are placed at distances of 3.2 mm, 2.6 mm and 2.0 mm from the plate. The defect dimensions are fixed at 8 mm in length and 0.2 mm in width. The simulation modelling diagram is shown in Figure 27.

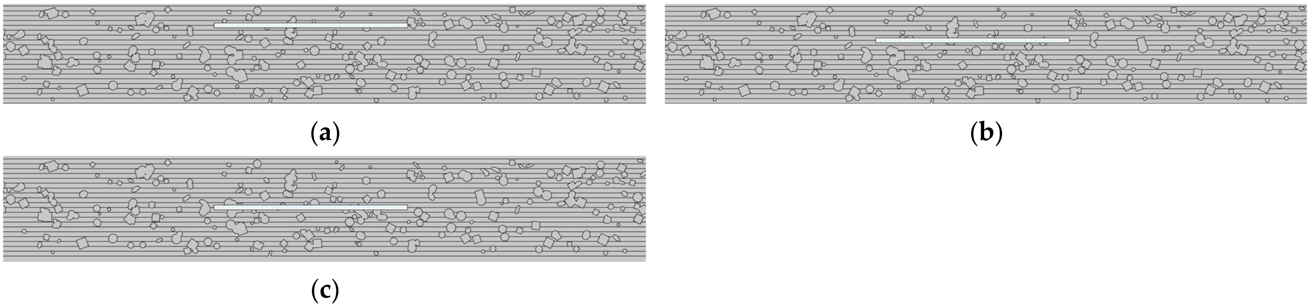

Figure 27. Simulation model diagrams at different stratification positions from the surface: (**a**) at 3.6 mm, (**b**) at 2.6 mm, (**c**) at 2.0 mm.

Figure 28 displays the time-domain signal of the Lamb wave l acquired at the receiving station, showing the variation in position along the depth direction of the layered defect. It can be observed that as the sublayer thickness decreases, the amplitude of the received signal increases significantly. The peak amplitude is highest at the 3.2 mm condition, after which the signal amplitude gradually diminishes with increasing depth of the defect. The reason for the above phenomenon is that as the layered position approaches the surface, dividing the original plate into two sections results in the thicker portion having a thickness increasingly consistent with that of the original plate. Consequently, the excitation conditions for Lamb waves within this section of the plate become increasingly similar to the original excitation conditions. In summary, the position of delamination defects in the depth direction can influence the propagation conditions of Lamb waves by regulating the thickness of the plate. Primarily, the closer the layered defect is to the surface of the plate, the lesser its impact on the propagation of Lamb waves within the plate.

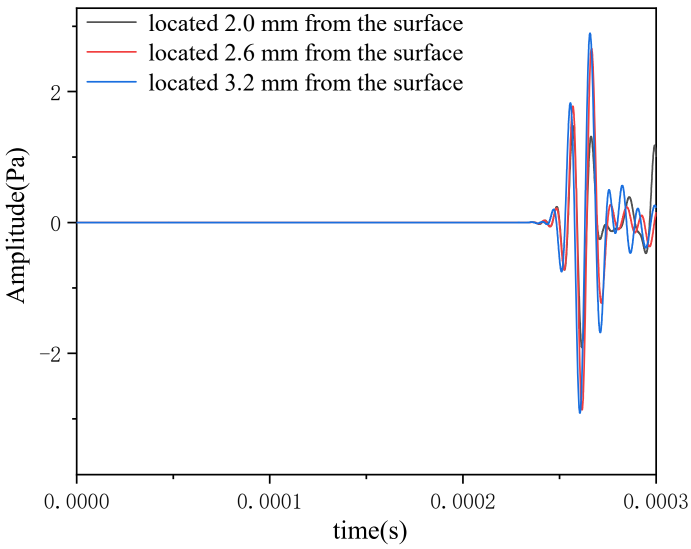

Figure 28. *Cont.*

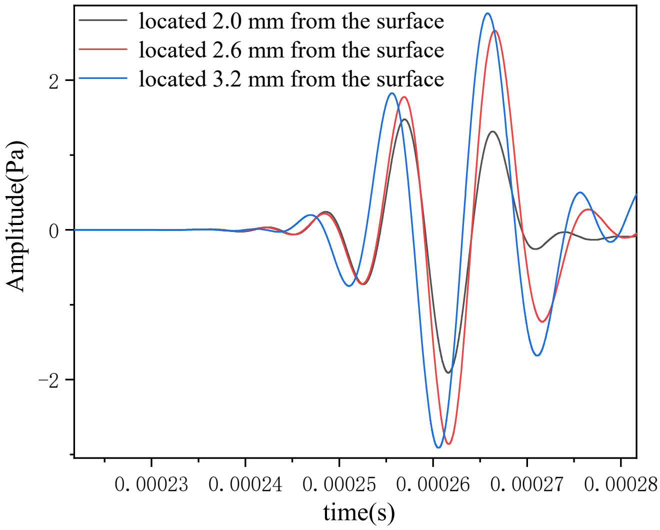

Figure 28. Time-domain diagram and enlarged view enlargement under conditions of delamination defects at different positions (2.0 mm, 2.6 mm and 1.6 mm from the surface respectively).

5. Conclusions

In this study, numerical simulations are employed to investigate the non-destructive testing of delamination defects in porous multilayer composite panels using Lamb waves. A CMC structure with 0° and 90° cross-laminated layers is established, random porosity is modeled within the plate, and an excitation model for the A_0 mode Lamb wave is developed based on the corresponding dispersion curve. The group velocity of the received signal is calculated, confirming that the A_0 mode Lamb wave is successfully excited through the finite element model established in this paper. The influence of porosity on Lamb wave propagation is analyzed, and the results indicate that the presence of porosity can lead to the attenuation of the signal. The effects of layered structures at different positions and lengths on the Lamb wave are compared and analyzed, results indicate that as the length of the layered defect increases and the defect position approaches the center of the plate, the attenuation of Lamb waves becomes more pronounced. The feasibility and sensitivity of utilizing air-coupled Lamb wave for detecting delamination defects in composite plates have been validated, providing a foundation for the non-destructive testing of laminated composite plates in applications.

Author Contributions: D.K., Conceptualization, resources, visualization; L.L., methodology, software, formal analysis, data curation, writing- original draft, visualization; Z.Z., Conceptualization, validation, supervision, funding acquisition; Y.Z., Conceptualization, validation; H.Z., validation, investigation; W.Z., writing—review and editing, supervision, project administration. All authors have read and agreed to the published version of the manuscript.

Funding: This research is funded by National Natural Science Foundation of China. grant number U23A20636.

Data Availability Statement: The data presented in this study are available on request from the corresponding author due to legal constraints.

Conflicts of Interest: The authors declare no conflict of interest.

References

1. Schmidt, S.; Beyer, S.; Knabe, H.; Immich, H.; Meistring, R.; Gessler, A. Advanced Ceramic Matrix Composite Materials for Current and Future Propulsion Technology Applications. *Acta Astronaut.* **2004**, *55*, 409–420. [CrossRef]

2. Zhang, D.-D.; Ren, J.; Gu, J. Nondestructive Testing of Bonding Defects in Multilayered Ceramic Matrix Composites Using THz Time Domain Spectroscopy and Imaging. *Compos. Struct.* **2020**, *251*, 112624. [CrossRef]
3. Wang, F.; Teng, X.; Hu, X.; Jiang, Y.; Guo, X.; Li, L.; Liu, X.; Liu, X.; Lu, H. Damage and Failure Analysis of a SiCf/SiC Ceramic Matrix Composite Using Digital Image Correlation and Acoustic Emission. *Ceram. Int.* **2022**, *48*, 4699–4709. [CrossRef]
4. Bolotin, V.V. Delaminations in Composite Structures: Its Origin, Buckling, Growth and Stability. *Compos. Part B* **1996**, *27*, 129–145. [CrossRef]
5. Han, D.-H.; Kang, L.-H. Nondestructive Evaluation of GFRP Composite Including Multi-Delamination Using THz Spectroscopy and Imaging. *Compos. Struct.* **2018**, *185*, 161–175. [CrossRef]
6. Dassios, K.G.; Kordatos, E.Z.; Aggelis, D.G.; Matikas, T.E. Nondestructive Damage Evaluation in Ceramic Matrix Composites for Aerospace Applications. *Sci. World J.* **2013**, *2013*, 715945. [CrossRef]
7. Laureti, S.; Bison, P.; Ferrarini, G.; Zito, R.; Ricci, M. Simultaneous Multi-Frequency Lock-in Thermography: A New Flexible and Effective Active Thermography Scheme. *NDT E Int.* **2024**, *146*, 103144. [CrossRef]
8. Mei, H.; Tan, Y.; Chang, P.; Xiao, S.; Huang, W.; Cheng, L. Simplified Approach to Study Oxidative Damage of C/SiC Composites Induced from Notch Defects. *Ceram. Int.* **2019**, *45*, 22464–22470. [CrossRef]
9. Chen, G.; Xia, J. Non-Contact Shear Wave Generation and Detection Using High Frequency Air-Coupled Focused Transducer and Fiber Optic Based Sagnac Interferometer for Mechanical Characterization. *Sensors* **2022**, *22*, 5824. [CrossRef]
10. Kazys, R.J.; Vilpisauskas, A.; Sestoke, J. Application of Air-Coupled Ultrasonic Arrays for Excitation of a Slow Antisymmetric Lamb Wave. *Sensors* **2018**, *18*, 2636. [CrossRef]
11. Kažys, R.; Demčenko, A.; Žukauskas, E.; Mažeika, L. Air-Coupled Ultrasonic Investigation of Multi-Layered Composite Materials. *Ultrasonics* **2006**, *44*, e819–e822. [CrossRef]
12. Malkin, R.; Kappus, B.; Long, B.; Price, A. On the Non-Linear Behaviour of Ultrasonic Air-Borne Phased Arrays. *J. Sound Vib.* **2023**, *552*, 117644. [CrossRef]
13. Eremin, A.; Glushkov, E.; Glushkova, N.; Lammering, R. Guided Wave Time-Reversal Imaging of Macroscopic Localized Inhomogeneities in Anisotropic Composites. *Struct. Health Monit.* **2019**, *18*, 1803–1819. [CrossRef]
14. Rose, J.L. *Ultrasonic Guided Waves in Solid Media*; Cambridge University Press: Cambridge, UK, 2014. [CrossRef]
15. Peng, K.; Zhang, Y.; Xu, X.; Han, J.; Luo, Y. Crack Detection of Threaded Steel Rods Based on Ultrasonic Guided Waves. *Sensors* **2022**, *22*, 6885. [CrossRef] [PubMed]
16. Xu, B.; Huang, J.; Jie, Y. Application of the Lamb Wave Mode of Acoustic Emission for Monitoring Impact Damage in Plate Structures. *Sensors* **2023**, *23*, 8611. [CrossRef]
17. Fariñas, M.D.; Calás, H.; Álvarez-Arenas, T.E.G. Visualization of Lamb Wave Propagation in Uncured CFRP and Curved Surfaces Using Air-Coupled Ultrasound. In Proceedings of the 2012 IEEE International Ultrasonics Symposium, Dresden, Germany, 7–10 October 2012; pp. 1429–1432. [CrossRef]
18. Kazys, R.J.; Vilpisauskas, A. Air-Coupled Reception of a Slow Ultrasonic A0 Mode Wave Propagating in Thin Plastic Film. *Sensors* **2020**, *20*, 516. [CrossRef] [PubMed]
19. Fan, Z.; Zhou, Y.; Wu, T.; Peng, P. The excitation and detection of lamb waves in a droplet-loaded plate using air-coupled ultrasonic transducers. *Measurement* **2021**, *172*, 108954. [CrossRef]
20. Roßdeutscher, J.; Mechnich, P.; Flucht, F.; Shi, Y.; Jemmali, R. Mechanical and Microstructural Assessment of Inhomogeneities in Oxide Ceramic Matrix Composites Detected by Air-Coupled Ultrasound Inspection. *J. Compos. Sci.* **2021**, *5*, 286. [CrossRef]
21. Krödel, S.; Palermo, A.; Daraio, C. Acoustic Properties of Porous Microlattices from Effective Medium to Scattering Dominated Regimes. *J. Acoust. Soc. Am.* **2018**, *144*, 319–329. [CrossRef]
22. Sun, J.; Ye, D.; Zou, J.; Chen, X.; Wang, Y.; Yuan, J.; Liang, H.; Qu, H.; Binner, J.; Bai, J. A Review on Additive Manufacturing of Ceramic Matrix Composites. *J. Mater. Sci. Technol.* **2023**, *138*, 1–16. [CrossRef]
23. Yeh, C.-H.; Yang, C.-H. Characterization of Mechanical and Geometrical Properties of a Tube with Axial and Circumferential Guided Waves. *Ultrasonics* **2011**, *51*, 472–479. [CrossRef]
24. Caldwell, R.A.; Feeny, B.F. Smooth Complex Orthogonal Decomposition Applied to Traveling Waves in Elastic Media. In *Proceedings of the Rotating Machinery, Hybrid Test Methods, Vibro-Acoustics & Laser Vibrometry, Volume 8*; De Clerck, J., Epp, D.S., Eds.; Springer International Publishing: Cham, Switzerland, 2016; pp. 281–293. [CrossRef]